Nonlinear Analysis: Modelling and Control, Vol. 27, No. 2, 308–330
https://doi.org/10.15388/namc.2022.27.25338

Vilnius University Press

Heat and mass source effect on MHD double-diffusive mixed convection and entropy generation in a curved enclosure filled with nanofluid

Rujda Parveen[1], **Tapas Ray Mahapatra**[2,3]

Department of Mathematics, Visva-Bharati (A Central University),
Santiniketan-731 235, West-Bengal, India
rujdaparveen7@gmail.com; trmahapatra@yahoo.com

Received: January 23, 2021 / **Revised:** June 19, 2021 / **Published online:** January 6, 2022

Abstract. This paper examines the two-dimensional laminar steady magnetohydrodynamic double-diffusive mixed convection in a curved enclosure filled with different types of nanofluids. The enclosure is differentially heated and concentrated, and the heat and mass source are embedded in a part of the left wall having temperature $T_h\ (>T_c)$ and concentration $c_h\ (>c_c)$. The right vertical wall is allowed to move with constant velocity in a vertically upward direction to cause a shear-driven flow. The governing equations along with the boundary conditions are transformed into a nondimensional form and are written in stream function-velocity formulation, which is then solved numerically using the Bi-CGStab method. Based on the numerical results, the effects of the dominant parameters such as Richardson number ($1 \leqslant Ri \leqslant 50$), Hartmann number ($0 \leqslant Ha \leqslant 60$), solid volume fraction of nanoparticles ($0.0 \leqslant \phi \leqslant 0.02$), location and length of the heat and mass source are examined. Results indicate that the augmentation of Richardson number, heat and mass source length and location cause heat and mass transfer to increase, while it decreases when Hartmann number and volume fraction of the nanoparticles increase. The total entropy generation rises by 1.32 times with the growing Richardson number, decreases by 1.21 times and 1.02 times with the rise in Hartmann number and nanoparticles volume fraction, respectively.

Keywords: magneto-hydrodynamics, complex enclosure flow, mixed convection, discrete heat source, entropy generation, double-diffusive, nanofluid.

1 Introduction

In the engineering and industrial context, a wide range of investigations has been performed for natural convection using nanofluid media with various techniques to improve the thermal conductivity and enhance the heat transfer performance of the fluid within the enclosure. To improve thermal behavior, numerous approaches have been proposed

[1]The author was supported by Department of Science and Technology (DST) INSPIRE, India
[2]The author was supported by SAP (DRS Phase-III) under UGC, New Delhi, India
[3]Corresponding author.

involving enclosure geometry, boundary conditions, filled media, etc. Nanofluid is defined as nanoscale particles (diameter less than 100 nm) or fibers diluted in a base fluid. In the literature, numerous studies have been conducted on the heat transfer and flow inside an enclosure filled with nanofluid medium [3, 34]. Heat transfer and Ag-water nanofluid flow inside a square enclosure with a center heater is analyzed by Mahalakshmi et al. [16]. Their outcomes indicate that an increase in heater length leads to an increase in heat transfer rate. Conjugate natural convection flow in a square cavity in presence of hybrid nanofluid is investigated by Ghalambaz et al. [9]. They stated that the heat transfer rate rises due to the rise in hybrid nanoparticles and thermal conductivity ratio. Natural convection of Ag-MgO hybrid/water nanofluid inside a porous enclosure by applying Darcy model is studied by Mehryan et al. [23]. They concluded that the heat transport decreases due to the dispersion of hybrid nanoparticles in the base fluid. Balushi et al. [2] considered a nonhomogeneous dynamic model to investigate natural convection by using magnetic nanoparticles in a square enclosure. They found that the average Nusselt number augments as the nanoparticles volume fraction increase.

There are several cases of heat transfer under the impact of the magnetic field because of their various variety of application in engineering areas such as chemical industry, power and cooling industry for drying, chemical vapor deposition on surfaces, cooling of nuclear reactors, crystal growth in liquids, cooling of nuclear reactors, electronic packages, and petroleum industries. From the works of literature, the influence of the magnetic field on the natural convection inside the enclosure decreases the convection effect and reduces the heat transfer rate. Therefore, the interaction of nanoparticles and the addition of nanoparticles to the fluid can improve its thermal performance (since the thermal conductivity of solid is typically higher than that of liquids) and heat transfer mechanism in the enclosure. Ghasemi et al. [10] was the first to use nanofluid (Al_2O_3-water) as the working fluid in the presence of a magnetic field in a differentially heated square enclosure. Their result showed that the presence of a magnetic field adversely affects the fluid flow, and heat transfer rate increases and decreases with the increase of the Rayleigh number and Hartmann number, respectively. Extensive research has been performed considering the effect of magnetic fields on fluid flow inside a cavity [15, 30].

There are several studies in the literature based on the phenomena of mixed convection inside enclosures [4, 12, 17, 19]. Öztop and Salem [26] carried a review on entropy generation in natural and mixed convection heat transfer. Mahapatra et al. [18] analyzed the effect of buoyancy ratio on double-diffusive mixed convection with uniform and nonuniform heating of walls in a lid-driven square enclosure. Double-diffusive mixed convection under the influence of the magnetic field has been investigated by Uddin et al. [33] for both uniformly and nonuniformly heated and concentrated walls. Double-diffusive mixed convection in a shallow inclined cavities with different inclination angles, Lewis numbers, and buoyancy ratios is numerically performed by Teamah et al. [32]. They observed that the mass transfer rate increases by increasing Lewis number, but there is no change in heat transfer rate. Also, the average Nusselt number and Sherwood number enhance with the rise in the buoyancy ratio.

Natural convection heat transfer in corrugated or wavy enclosures is gaining the attention of most researchers for enhancing the efficiency of heat and mass transfer. Over

the last few years, natural convection in complex enclosures has been carried out by various researchers [20, 25, 31]. Rahimpour and Moraveji [28] examined the heat transfer of MHD free convection in a C-shaped chamber filled with Fe_3O_4/water nanofluids. They examined the impact of Hartmann, Rayleigh numbers, chamber tilted angle, nanoparticles concentration, and chamber geometrical parameter on thermal performance and fluid flow structures. Rashed et al. [29] carried out the buoyancy-driven flow of hybrid nanofluids within an inclined two-sided wavy enclosure considering magneto-convection flow. Bezi et al. [5] studied the entropy generation and heat transfer flow in a semiannular enclosure filled with nanofluid. Their results show that the entropy generation strengthened by increasing the Rayleigh number. Ahmed [1] performed natural convection of dusty hybrid nanofluids in diverging-converging cavities including volumetric heat sources. The heat transfer of MHD flow of Newtonian nanoliquid in a baffled U-shaped enclosure is investigated by Zaim et al. [35]. The Fe_3O_4-H_2O nanofluid flow inside a Novel shape porous cavity is examined by Molana et al. [24] subjected to magnetic-field-dependent viscosity. They deduced that the Nusselt number has a direct relationship with the aspect ratio. Chamkha et al. [7] investigated the entropy generation of nanofluid flow inside a gamma-shaped porous cavity considering the magnetic field. They found that by raising the nanoparticle volume fraction the heat transfer rate and entropy generation enhance.

From our investigations there are limited attempts focused on mixed convection flow inside a complex enclosure filled with nanofluid. Thus, the aim of the present work is to investigate the steady MHD double-diffusive mixed convection in a curved enclosure filled with nanofluid. The reasons for selecting this model are:

- Importance of this curved fluid flow geometry (or curved duct) [8, 13, 21] in many engineering and technological systems such as compact heat exchangers, steam boilers, thermal power generation, aircraft engines, etc.
- Its originality since limited work has been done in such geometry considering double-diffusive mixed convection as the mode of heat transfer and nanofluid as the medium.

The influence of Richardson number, the solid volume fraction of nanoparticles, the type of nanofluids, and heat and mass source length and location on the average Nusselt number, Sherwood number, and total entropy generation have been studied. This paper is organized as follows. Section 2 presents the physical model. Section 3 includes mathematical formulation. Section 4 discusses the numerical implementation and code validation. Section 5 presents the results and discussion. Finally, a conclusion is given in Section 6.

2 Physical model

The schematic diagram of the system considered in this paper is depicted in Fig. 1. The enclosure is of length L, and a discrete heat and concentration source of dimensionless length H are located at the left wall of the enclosure having constant hot temperature T_h and concentration c_h. The remaining part of the left wall and the right wall are considered to be at constant temperature and concentration of $T_c\ (< T_h)$ and $c_c\ (< c_h)$, respectively. The top and bottom walls are assumed to be adiabatic and impermeable. Furthermore,

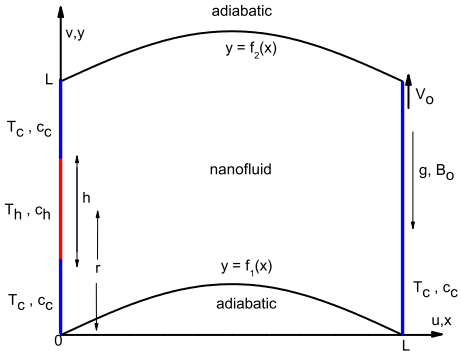

Figure 1. Schematic representation of geometry and boundary conditions in dimensional form.

the right wall of the enclosure is allowed to move in upward direction with a constant velocity of V_0, while all the remaining walls are at rest. An external magnetic field with uniform strength B_0 and the gravitational force g are applied in the vertically downward direction. The fluid inside the enclosure is a water-based nanofluid containing different types of nanoparticles such as Cu, Ag, Al_2O_3, and TiO_2. There is no slip between the particles of the base fluid and the nanoparticles, and they are assumed to be in thermal equilibrium. In dimensional form, the lower and upper wall of the enclosure is defined by the functions

$$f_1(x) = a\sin\left(\pi\frac{x}{L}\right), \qquad f_2(x) = L + a\sin\left(\pi\frac{x}{L}\right),$$

where a is the amplitude of the sinusoidal walls. The nanofluid is considered to be Newtonian, and the flow is steady, incompressible, and viscous.The viscous dissipation and magnetic dissipation are expected to be negligible.The flow is directed by a combined buoyancy effect due to both temperature and concentration variations. The density variation is described by the following formula:

$$\rho = \rho_0\big[1 - \beta_T(T - T_c) - \beta_s(c - c_c)\big],$$

where T and c are the dimensional temperature and solute concentration, respectively, and ρ, β_T, β_s are the fluid density, volumetric coefficient of thermal expansion, and volumetric coefficient of solutal expansion, respectively.

3 Mathematical formulations

3.1 Thermo-physical properties of nanofluid

The thermo-physical properties of the base fluid and nano-sized particles are tabulated in Table 1, where C_p, k, σ, μ, and α indicate the specific heat, thermal conductivity, electrical conductivity, dynamic viscosity, and thermal diffusivity, respectively.

Table 1. Thermophysical properties of the base fluid (pure water) and nanoparticle.

Properties	Pure water	Al_2O_3	Cu	Ag	TiO_2
C_p $(\mathrm{J\,kg^{-1}K^{-1}})$	4179	765	385	235	686.2
k $(\mathrm{W\,m^{-1}K^{-1}})$	0.623	40	400	429	8.9538
ρ $(\mathrm{kg\,m^{-3}})$	997.1	3970	8933	10500	4250
β_T $(\mathrm{K^{-1}})$	$21 \cdot 10^{-5}$	$0.8 \cdot 10^{-5}$	$1.67 \cdot 10^{-5}$	$1.8 \cdot 10^{-5}$	$0.9 \cdot 10^{-5}$
σ $(\mathrm{kg^{-1}m^{-3}s^3A^2})$	0.05	$3.69 \cdot 10^7$	$5.69 \cdot 10^7$	$6.30 \cdot 10^7$	$2.38 \cdot 10^6$
μ $(\mathrm{kg\,m^{-1}s^{-1}})$	0.001003	–	–	–	–
α $(\mathrm{m^2s^{-1}})$	$0.143 \cdot 10^{-6}$	–	–	–	–

The effective density ρ_{nf}, specific heat $(\rho C_p)_{nf}$, thermal expansion coefficient $(\rho\beta)_{nf}$ of the nanofluid, according to [3], are:

$$(\rho_{nf}) = (1-\phi)\rho_f + \phi\rho_s, \qquad (\rho C_p)_{nf} = (1-\phi)(\rho C_p)_f + \phi(\rho C_p)_s$$

and

$$(\rho\beta_T)_{nf} = (1-\phi)(\rho\beta_T)_f + \phi(\rho\beta_T)_s.$$

Effective dynamic viscosity μ_{nf} and the effective thermal conductivity k_{nf} of the nanofluid, which are obtained from Brinkman model [6] and Maxwell's model [22], respectively, are introduced as

$$\mu_{nf} = \mu_f(1-\phi)^{-2.5} \quad \text{and} \quad k_{nf} = k_f\left(\frac{k_s + 2k_f - 2\phi(k_f - k_s)}{k_s + 2k_f + \phi(k_f - k_s)}\right).$$

Finally, the thermal diffusivity and electrical conductivity of the nanofluid are defined, respectively, as

$$\alpha_{nf} = \frac{k_{nf}}{(\rho C_p)_{nf}} \quad \text{and} \quad \sigma_{nf} = \sigma_f\left(1 + \frac{3(\zeta-1)\phi}{(\zeta+2) - (\zeta-1)\phi}\right).$$

Here ϕ represents the volume fraction of the nanoparticle, and $\zeta = \sigma_s/\sigma_f$. The subscripts f, s, and nf are used to refer base fluid, solid particle, and nanofluid, respectively.

3.2 Governing equations

The equations, which govern the double-diffusive flow, are given in dimensional form [4].

Continuity equation:

$$\frac{\partial u}{\partial x} + \frac{\partial v}{\partial y} = 0. \tag{1}$$

Momentum conservation equations:

$$u\frac{\partial u}{\partial x} + v\frac{\partial u}{\partial y} = -\frac{1}{\rho_{nf}}\frac{\partial p}{\partial x} + \nu_{nf}\left[\frac{\partial^2 u}{\partial x^2} + \frac{\partial^2 u}{\partial y^2}\right] - \frac{\sigma_{nf}\, B_0^2\, u}{\rho_{nf}}, \tag{2}$$

$$u\frac{\partial v}{\partial x} + v\frac{\partial v}{\partial y} = -\frac{1}{\rho_{nf}}\frac{\partial p}{\partial y} + \nu_{nf}\left[\frac{\partial^2 v}{\partial x^2} + \frac{\partial^2 v}{\partial y^2}\right] + \frac{g(\rho\beta_T)_{nf}}{\rho_{nf}}(T - T_c). + \frac{g(\rho\beta_S)_{nf}}{\rho_{nf}}(c - c_c). \tag{3}$$

Energy equation:

$$u\frac{\partial T}{\partial x}+v\frac{\partial T}{\partial y}=\alpha_{nf}\left[\frac{\partial^2 T}{\partial x^2}+\frac{\partial^2 T}{\partial y^2}\right]. \tag{4}$$

Concentration equation:

$$u\frac{\partial c}{\partial x}+v\frac{\partial c}{\partial y}=D\left[\frac{\partial^2 c}{\partial x^2}+\frac{\partial^2 c}{\partial y^2}\right]. \tag{5}$$

Here u and v are the dimensional velocities along the x and y directions, p represents the dimensional fluid pressure, and D is the mass diffusivity.

Following transformation of variables are used to convert system (1)–(5) into nondimensional form:

$$\begin{aligned} &X=\frac{x}{L}, \qquad Y=\frac{y}{L}, \qquad U=\frac{u}{V_0}, \qquad V=\frac{v}{V_0},\\ &P=\frac{p}{\rho_{nf}V_0^2}, \qquad \theta=\frac{T-T_c}{T_h-T_c}, \qquad C=\frac{c-c_c}{c_h-c_c}. \end{aligned} \tag{6}$$

The resulting nondimensional continuity, momentum, energy, and concentration equations can be written as

$$\frac{\partial U}{\partial X}+\frac{\partial V}{\partial Y}=0,$$

$$U\frac{\partial U}{\partial X}+V\frac{\partial U}{\partial Y}=-\frac{\partial P}{\partial X}+\frac{\mu_{nf}}{\rho_{nf}\nu_f}\frac{1}{Re}\left[\frac{\partial^2 U}{\partial X^2}+\frac{\partial^2 U}{\partial Y^2}\right]-\frac{\sigma_{nf}\rho_f}{\sigma_f\rho_{nf}}\frac{Ha^2}{Re}U, \tag{7}$$

$$U\frac{\partial V}{\partial X}+V\frac{\partial V}{\partial Y}=-\frac{\partial P}{\partial Y}+\frac{\mu_{nf}}{\rho_{nf}\nu_f}\frac{1}{Re}\left[\frac{\partial^2 V}{\partial X^2}+\frac{\partial^2 V}{\partial Y^2}\right]+\frac{(\rho\beta_T)_{nf}}{\rho_{nf}\beta_f}\,Ri(\theta+NC), \tag{8}$$

$$U\frac{\partial \theta}{\partial X}+V\frac{\partial \theta}{\partial Y}=\frac{\alpha_{nf}}{\alpha_f}\frac{1}{RePr}\left[\frac{\partial^2 \theta}{\partial X^2}+\frac{\partial^2 \theta}{\partial Y^2}\right], \tag{9}$$

$$U\frac{\partial C}{\partial X}+V\frac{\partial C}{\partial Y}=\frac{1}{LeRePr}\left[\frac{\partial^2 C}{\partial X^2}+\frac{\partial^2 C}{\partial Y^2}\right],$$

where U and V are the dimensionless velocities along the X and Y directions, P, θ, and C represent the dimensionless pressure, temperature, and concentration, respectively.

The nondimensional parameters are given by

$$\begin{aligned} &Pr=\frac{\nu_f}{\alpha_f}, \qquad Le=\frac{\alpha_f}{D}, \qquad Gr=\frac{g\,\beta_f(T_h-T_c)L^3}{\nu_f^2}, \qquad Re=\frac{V_0L}{\nu_f},\\ &Ha=\sqrt{\frac{\sigma_f}{\mu_f}}B_0L, \qquad Ri=\frac{Gr}{Re^2}, \qquad N=\frac{(\rho\beta_s)_{nf}(c_h-c_c)}{(\rho\beta_T)_{nf}(T_h-T_c)}, \end{aligned}$$

where Pr, Le, Gr, Re, Ha, Ri, and N are Prandtl number, Lewis number, Grashof number, Reynolds number, Hartmann number, Richardson number, and buoyancy ratio, respectively.

The lower and upper sinusoidal wall in nondimensional form can be written as

$$F_1(X) = A\sin(\pi X), \qquad F_2(X) = 1 + A\sin(\pi X),$$

where $A = a/L(= 0.2)$ is the dimensionless amplitude of the sinusoidal walls.

The imposed boundary conditions on the enclosure in nondimensional form on top and bottom wall:

$$U = V = 0, \quad \frac{\partial\theta}{\partial Y} = \frac{\partial C}{\partial Y} = 0;$$

on right wall:

$$U = 0, \quad V = 1, \quad \theta = 0 = C, \quad X = 1;$$

on left wall:

$$U = 0, \quad V = 0;$$

having heat and mass source:

$$\theta = 1 = C \quad \text{for } R - \frac{H}{2} \leqslant Y \leqslant R + \frac{H}{2},\ X = 0;$$

without heat and mass source:

$$\theta = 0 = C \quad \text{for } 0 \leqslant Y < R - \frac{H}{2},\ R + \frac{H}{2} < Y \leqslant 1,\ X = 0.$$

Here $R = r/L$ and $H = h/L$.

3.3 Nusselt number and Sherwood number

The local Nusselt number Nu and local Sherwood number Sh at the left wall is defined as

$$Nu = -\frac{k_{nf}}{k_f}\frac{\partial\theta}{\partial X} \quad \text{and} \quad Sh = -\frac{\partial C}{\partial X}.$$

The average Nusselt number Nu_{avg} and average Sherwood number Sh_{avg} are obtained by integrating local Nusselt number Nu and local Sherwood number Sh, respectively:

$$Nu_{\text{avg}} = \int_{R-H/2}^{R+H/2} Nu\,\mathrm{d}Y \quad \text{and} \quad Sh_{\text{avg}} = \int_{R-H/2}^{R+H/2} Sh\,\mathrm{d}Y.$$

To evaluate the integrals, a Simpson's $(1/3)$rd rule of integration is implemented.

3.4 Governing equations for entropy generation

The boundary conditions imposes nonequilibrium flow in the flow field that causes entropy generation. The local entropy generation equations in dimensional form are

$$
\begin{aligned}
s_\theta &= \frac{k_{nf}}{T_0^2}\left[\left(\frac{\partial T}{\partial x}\right)^2+\left(\frac{\partial T}{\partial y}\right)^2\right],\\
s_\psi &= \frac{\mu_{nf}}{T_0}\left[2\left(\left(\frac{\partial u}{\partial x}\right)^2+\left(\frac{\partial v}{\partial y}\right)^2\right)+\left(\frac{\partial u}{\partial y}+\frac{\partial v}{\partial x}\right)^2\right],\\
s_m &= \frac{\sigma_{nf}}{T_0}B_o^2U^2,\\
s_d &= \frac{R_cD}{c_0}\left[\left(\frac{\partial c}{\partial x}\right)^2+\left(\frac{\partial c}{\partial y}\right)^2\right]+\frac{R_cD}{c_0}\left[\left(\frac{\partial c}{\partial x}\right)\left(\frac{\partial T}{\partial x}\right)+\left(\frac{\partial c}{\partial y}\right)\left(\frac{\partial T}{\partial y}\right)\right],
\end{aligned}
$$

where s_θ, s_ψ, s_m, and s_d are entropy generation due to heat transfer, fluid friction, magnetic field, and solutal concentration, respectively. The dimensionless forms of the local entropy generation expression using the dimensionless quantities in (6) are given by

$$
\begin{aligned}
S_\theta &= \frac{k_{nf}}{k_f}\left[\left(\frac{\partial \theta}{\partial X}\right)^2+\left(\frac{\partial \theta}{\partial Y}\right)^2\right],\\
S_\psi &= \lambda_1\frac{\mu_{nf}}{\mu_f}\left[2\left(\left(\frac{\partial U}{\partial X}\right)^2+\left(\frac{\partial V}{\partial Y}\right)^2\right)+\left(\frac{\partial U}{\partial Y}+\frac{\partial V}{\partial X}\right)^2\right],\\
S_m &= \lambda_1\frac{\sigma_{nf}}{\sigma_f}Ha^2U^2,\\
S_d &= \lambda_2\left[\left(\frac{\partial C}{\partial X}\right)^2+\left(\frac{\partial C}{\partial Y}\right)^2\right]+\lambda_3\left[\left(\frac{\partial C}{\partial X}\right)\left(\frac{\partial \theta}{\partial X}\right)+\left(\frac{\partial C}{\partial Y}\right)\left(\frac{\partial \theta}{\partial Y}\right)\right],
\end{aligned}
$$

where

$$
\lambda_1 = \frac{\mu_f T_0}{k_f}\left(\frac{V_0}{(T_h-T_c)}\right)^2, \qquad \lambda_2 = \frac{R_cDT_0}{k_fC_0}\left(\frac{c_h-c_c}{T_h-T_c}\right)^2,
$$
$$
\lambda_3 = \frac{R_cD}{k_f}\left(\frac{c_h-c_c}{T_h-T_c}\right)
$$

are called irreversibility distribution ratios and taken as $\lambda_1 = 0.0001$, $\lambda_2 = 0.5$, and $\lambda_3 = 0.01$. Here R_c is the gas constant, T_0 and C_0 are bulk temperature and bulk concentration, respectively, and could be calculated as $T_0 = (T_h + T_c)/2$ and $C_0 = (c_h + c_c)/2$, respectively.

The average entropy generation due to heat transfer $S_{\theta,\mathrm{avg}}$, fluid friction $S_{\psi,\mathrm{avg}}$, magnetic field $S_{m,\mathrm{avg}}$, and diffusion $S_{d,\mathrm{avg}}$ are obtained by integrating the local entropy

generation by the system volume:

$$S_{\theta,\mathrm{avg}} = \int_V S_\theta \,\mathrm{d}V, \qquad S_{\psi,\mathrm{avg}} = \int_V S_\psi \,\mathrm{d}V,$$
$$S_{m,\mathrm{avg}} = \int_V S_m \,\mathrm{d}V, \qquad S_{d,\mathrm{avg}} = \int_V S_d \,\mathrm{d}V.$$

The total entropy generation is given by $S_{\mathrm{total}} = S_{\theta,\mathrm{avg}} + S_{\psi,\mathrm{avg}} + S_{m,\mathrm{avg}} + S_{d,\mathrm{avg}}$.

4 Numerical technique

4.1 Methodology

The stream function ψ and vorticity ω in nondimensional form are given by

$$U = \frac{\partial \psi}{\partial Y}, \quad V = -\frac{\partial \psi}{\partial X}, \quad \text{and} \quad \omega = \frac{\partial V}{\partial X} - \frac{\partial U}{\partial Y}, \tag{10}$$

which gives a single equation

$$\frac{\partial^2 \psi}{\partial X^2} + \frac{\partial^2 \psi}{\partial Y^2} = -\omega. \tag{11}$$

Using Eq. (10) and eliminating pressure term from Eqs. (7) and (8), we get

$$\frac{\mu_{nf}}{\rho_{nf}\nu_f}\frac{1}{Re}\left(\frac{\partial^2 \omega}{\partial X^2} + \frac{\partial^2 \omega}{\partial Y^2}\right) - \left(U\frac{\partial \omega}{\partial X} + V\frac{\partial \omega}{\partial Y}\right) + \frac{(\rho\beta_T)_{nf}}{\rho_{nf}\beta_f} Ri\left(\frac{\partial \theta}{\partial X} + N\frac{\partial C}{\partial X}\right) + \frac{\sigma_{nf}\rho_f}{\sigma_f \rho_{nf}}\frac{Ha^2}{Re}\frac{\partial U}{\partial Y} = 0. \tag{12}$$

The presence of the curved walls make it difficult to impose the curve boundary on rectangular grids. Thus, transformation is required to convert the irregular physical domain (X, Y) into a regular (square) computational domain (ξ, η); see Fig. 2. In this study, we have considered the following coordinate transformation:

$$\xi = X, \qquad \eta = \frac{Y - F_1(X)}{F_2(X) - F_1(X)}.$$

Using the above transformation, the sinusoidal boundaries are transformed into the straight lines.

The equations can be evaluated in $\xi - \eta$ domain using the following relationship:

$$\begin{pmatrix} \frac{\partial \xi}{\partial X} & \frac{\partial \xi}{\partial Y} \\ \frac{\partial \eta}{\partial X} & \frac{\partial \eta}{\partial Y} \end{pmatrix} = \frac{1}{J}\begin{pmatrix} \frac{\partial Y}{\partial \eta} & -\frac{\partial X}{\partial \eta} \\ -\frac{\partial Y}{\partial \xi} & \frac{\partial X}{\partial \xi} \end{pmatrix}, \quad J = \frac{\partial(X,Y)}{\partial(\xi,\eta)} = \begin{vmatrix} \frac{\partial X}{\partial \xi} & \frac{\partial X}{\partial \eta} \\ \frac{\partial Y}{\partial \xi} & \frac{\partial Y}{\partial \eta} \end{vmatrix}.$$

Here J is the Jacobian of the transformation.

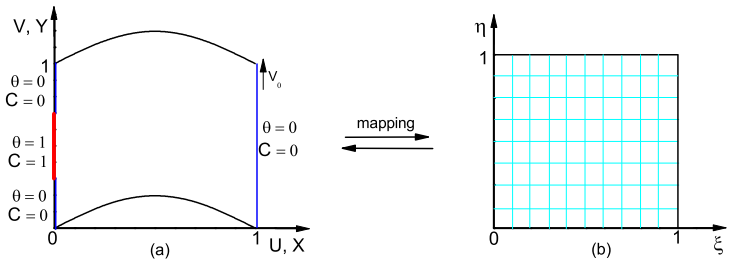

Figure 2. Mapping of physical domain (a) to computational domain (b).

Using the above relations, the governing equations (8), (9), (11), and (12) can be written in new transformed coordinates as

$$
\begin{aligned}
&a_3\frac{\partial^2\theta}{\partial\xi^2}+e_3\frac{\partial^2\theta}{\partial\xi\partial\eta}+b_3\frac{\partial^2\theta}{\partial\eta^2}+c_3\frac{\partial\theta}{\partial\xi}+d_3\frac{\partial\theta}{\partial\eta}=0,\\
&a_4\frac{\partial^2 C}{\partial\xi^2}+e_4\frac{\partial^2 C}{\partial\xi\partial\eta}+b_4\frac{\partial^2 C}{\partial\eta^2}+c_4\frac{\partial C}{\partial\xi}+d_4\frac{\partial C}{\partial\eta}=0,\\
&a_1\frac{\partial^2\psi}{\partial\xi^2}+e_1\frac{\partial^2\psi}{\partial\xi\partial\eta}+b_1\frac{\partial^2\psi}{\partial\eta^2}+c_1\frac{\partial\psi}{\partial\xi}+d_1\frac{\partial\psi}{\partial\eta}=-\omega, \qquad (13)\\
&a_2\frac{\partial^2\omega}{\partial\xi^2}+e_2\frac{\partial^2\omega}{\partial\xi\partial\eta}+b_2\frac{\partial^2\omega}{\partial\eta^2}+c_2\frac{\partial\omega}{\partial\xi}+d_2\frac{\partial\omega}{\partial\eta}+\frac{\sigma_{nf}\rho_f}{\sigma_f\rho_{nf}}\frac{Ha^2}{Re}\left(\frac{1}{J}\frac{\partial U}{\partial\eta}\right)\\
&\quad+\frac{(\rho\beta_T)_{nf}}{\rho_{nf}\beta_f}Ri\left[\left(\frac{\partial\theta}{\partial\xi}+\frac{e_1}{2}\frac{\partial\theta}{\partial\eta}\right)-N\left(\frac{\partial C}{\partial\xi}+\frac{e_1}{2}\frac{\partial C}{\partial\eta}\right)\right]=0, \qquad (14)
\end{aligned}
$$

where

$$U=\frac{1}{J}\frac{\partial\psi}{\partial\eta}\quad\text{and}\quad V=-\frac{\partial\psi}{\partial\xi}-\frac{e_1}{2}\frac{\partial\psi}{\partial\eta}.$$

We get the following biharmonic equation in stream function-velocity formulation by substituting ω from Eq. (13) and writing in (14):

$$
\begin{aligned}
&a_2\frac{\partial^4\psi}{\partial\xi^4}+2e_2\frac{\partial^4\psi}{\partial\xi^3\partial\eta}+T_1\frac{\partial^4\psi}{\partial\xi^2\partial\eta^2}+2e_2b_1\frac{\partial^4\psi}{\partial\xi\partial\eta^3}\\
&\quad+b_1b_2\frac{\partial^4\psi}{\partial\eta^4}+c_2\frac{\partial^3\psi}{\partial\xi^3}+T_2\frac{\partial^3\psi}{\partial\xi^2\partial\eta}+T_3\frac{\partial^3\psi}{\partial\xi\partial\eta^2}+T_4\frac{\partial^3\psi}{\partial\eta^3}\\
&\quad+T_5\frac{\partial^2\psi}{\partial\xi\partial\eta}+T_6\frac{\partial^2\psi}{\partial\eta^2}+T_7\frac{\partial\psi}{\partial\eta}-\frac{\sigma_{nf}\rho_f}{\sigma_f\rho_{nf}}\frac{Ha^2}{Re}\left(\frac{1}{J}\frac{\partial U}{\partial\eta}\right)\\
&\quad-\frac{(\rho\beta_T)_{nf}}{\rho_{nf}\beta_f}Ri\left[\left(\frac{\partial\theta}{\partial\xi}+\frac{e_1}{2}\frac{\partial\theta}{\partial\eta}\right)-N\left(\frac{\partial C}{\partial\xi}+\frac{e_1}{2}\frac{\partial C}{\partial\eta}\right)\right]=0.
\end{aligned}
$$

The calculations are performed in computational domain, and the results are then transformed back to the physical domain. The transformed equations are discretized using a second-order central difference scheme. The set of discretized equations for each variable are solved by using an outer-inner iteration procedure, biconjugate gradientstabilized

method (BiCGStab) [14, 27]. The tridiagonal system

$$\left(\frac{\partial\psi}{\partial\xi}\right)_{i+1,j} + 4\left(\frac{\partial\psi}{\partial\xi}\right)_{i,j} + \left(\frac{\partial\psi}{\partial\xi}\right)_{i-1,j} = \frac{3}{d}(\psi_{i+1,j} - \psi_{i-1,j}),$$
$$\left(\frac{\partial\psi}{\partial\eta}\right)_{i,j+1} + 4\left(\frac{\partial\psi}{\partial\eta}\right)_{i,j} + \left(\frac{\partial\psi}{\partial\eta}\right)_{i,j-1} = \frac{3}{d}(\psi_{i,j+1} - \psi_{i,j-1})$$

is solved by using Thomas algorithm to get $\partial\psi/\partial\xi$ and $\partial\psi/\partial\eta$. After obtaining $\partial\psi/\partial\xi$ and $\partial\psi/\partial\eta$, we compute U and V.

The numerical method was implemented in FORTRAN software. The convergence criterion is that the difference of values of all the variables between two consecutive iterations is less than $0.5 \cdot 10^{-6}$.

4.2 Code validation and grid independence study

Accuracy tests were made for $\psi_{\min}$ in Table 2 for grid independence using the four sets of grids: 21×21, 41×41, 81×81, and 161×161. A good agreement was found between 81×81 and 161×161 grids, so the numerical computations were carried out using 81×81 grid nodal points.

The present results have been authenticated successfully in three steps:

- With the work of Ghasemi et al. [10], for Nu_{avg}, using various Hartmann numbers in a differentially heated square cavity at $Pr = 6.2$, $\phi = 0.02$, and $Ra = 10^5$; shown in Table 3.
- With the result of Mahapatra et al. [18], in a square enclosure maintained at different temperatures and concentrations as represented in Figs. 3(a) and 3(b). The average Nusselt number and average Sherwood number at the lower wall were compared when $Pr = 0.7$, $Le = 2.0$, and $N = 1.0$ for various values of Rayleigh number.
- With the work of Gupta and Kalita [11], for $\psi_{\min}$, using various Reynolds numbers in a lid-driven square cavity; shown in Fig. 3(c).

It is clear from Table 3 and Fig. 3 that the obtained results of the present work illustrate good agreement with those from the earlier investigations, and therefore, we get the confidence of the present numerical code.

Table 2. Grid independence test for $\psi_{\min}$ at $Ha = 30$, $\phi = 0.01$, $Le = 2$, $H = 0.4$, $R = 0.5$, and $Ri = 10$.

Grid size	21×21	41×41	81×81	161×161
$\psi_{\min}$	-0.0201	-0.0211	-0.0267	-0.0235

Table 3. Comparison of the average Nusselt number Nu_{avg} with results of Ghasemi et al. [10].

	$Ha = 0$	$Ha = 15$	$Ha = 30$	$Ha = 45$	$Ha = 60$
Ghasemi et al. [10]	4.82	4.14	3.15	2.36	1.85
Present	4.78	4.07	3.11	2.32	1.83

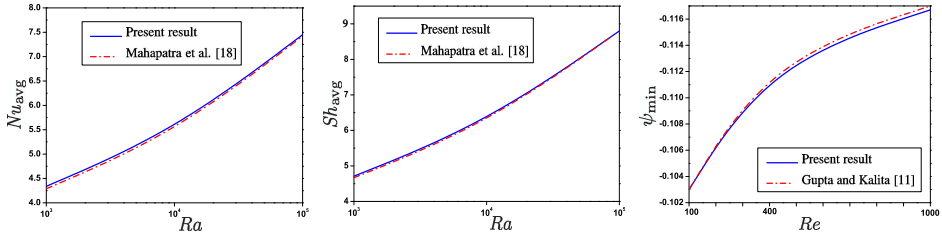

(a) (b) (c)

Figure 3. Comparison of present results: (a), (b) with Mahapatra et al. [18]; with (c) Gupta and Kalita [11].

5 Results and discussion

The present work investigated numerically MHD double-diffusive mixed convective heat and mass transfer and entropy generation in a curved enclosure filled with different types of nanofluids and subjected to discrete heating. The right wall is moving in an upward direction. The influence of various physical parameters such as Richardson number, Hartmann number, heat and mass source location and length, the volume fraction of nanoparticles are examined in terms of streamlines, isotherms, isoconcentrations, entropy generation, average Nusselt number, and average Sherwood number. We have carried out the simulation for fixed Prandtl number ($Pr = 6.2$), Reynolds number ($Re = 100$), and Buoyancy ratio ($N = 2$).

5.1 Effects of Richardson number

In the mixed convection problem, the Richardson number is used to show the importance of natural convection relative to the forced convection. It might be noticed that free convection phenomena are studied for $Ri > 10$, and mixed convection effects can be visualized for $Ri = 1$. Figure 4 describes the contour of streamlines, isotherms, and isoconcentrations for various values of Richardson number ($1 \leqslant Ri \leqslant 50$) inside the enclosure filled with Cu-water nanofluid ($\phi = 0.01$) at $Ha = 30$, $Le = 2$, $R = 0.5$, $H = 0.4$. At low Richardson number ($Ri = 1$), the thermal buoyancy forces and inertia forces are in balance. The distribution of streamlines shows the mixed convection effect with two counter-rotating vortices, and the isotherm and isoconcentration patterns are appeared to be linear. As the Richardson number increases ($Ri > 10$), the buoyancy forces predominate the inertia forces, and hence, the natural convection becomes more effective than mixed convection. From the figure it is observed that the secondary anticlockwise vortices adjacent to the right cold wall begin to vanish, and the enclosure is filled with primary clockwise vortices. The strength of fluid flow increases from $\psi_{\min} = -0.016$ for $Ri = 1$ to $\psi_{\min} = -0.283$ for $Ri = 50$. The isotherm and isoconcentration lines show a similar pattern due to similarity in energy and mass equation. They become irregular and spread in an upward direction signifying convection mode. The isoconcentration lines are found to be more compressed than isothermal lines resulting in a high mass transfer rate compared to heat transfer. From the observations we can conclude that the

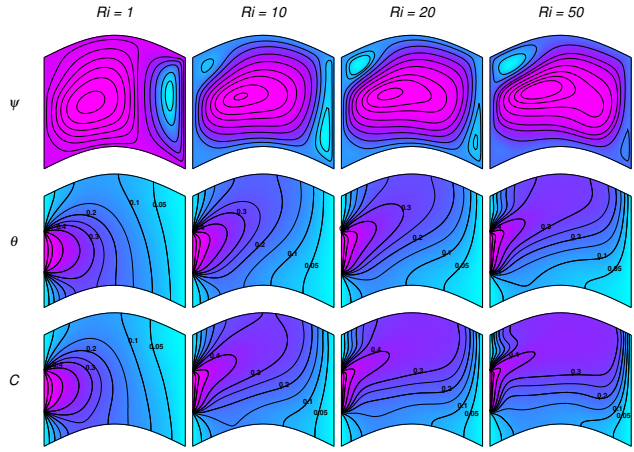

Figure 4. Streamlines, isotherms and isoconcentrations for different Ri at $Ha = 30$, $Le = 2$, $R = 0.5$, $H = 0.4$ and $\phi = 0.01$.

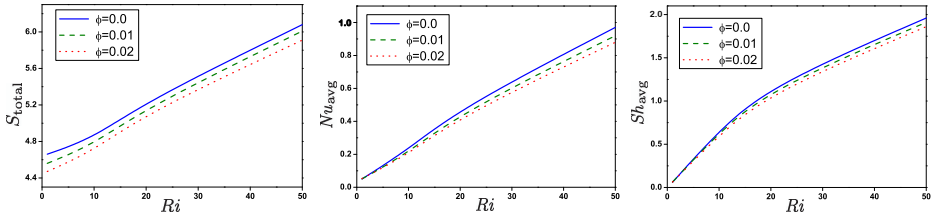

(a) (b) (c)

Figure 5. Variation of total entropy generation S_{total}, Nusselt number Nu_{avg} and Sherwood number Sh_{avg} for different values of Ri at $R = 0.5$, $H = 0.4$, $Ha = 30$ and $Le = 2$.

natural convection effect is dominating over the mixed convection. Figure 5(a) depicts the variation of total entropy generation with Ri. It is observed that S_{total} increases with Ri and is found to be high for pure fluid ($\phi = 0.0$) than nanofluid. The heat and mass transfer rate are determined using the average Nusselt Nu_{avg} and Sherwood Sh_{avg} numbers, respectively. From Figs. 5(b) and 5(c) it can be seen that irrespective of other parameters, the increase in Ri escalates Nu_{avg} and Sh_{avg} due to enhanced convection, and consequently, heat and mass transfer is increasing function of Richardson number. Also, the Nu_{avg} and Sh_{avg} decrease with the addition of nanoparticles.

5.2 Effects of Hartmann number

Figure 6 illustrates the effect of the magnetic field parameter Ha ($0 \leqslant Ha \leqslant 60$) in terms of streamlines, isotherms, and isoconcentrations. As seen from the figure, the flow field, temperature, and concentration distribution have an inverse relation with the magnetic

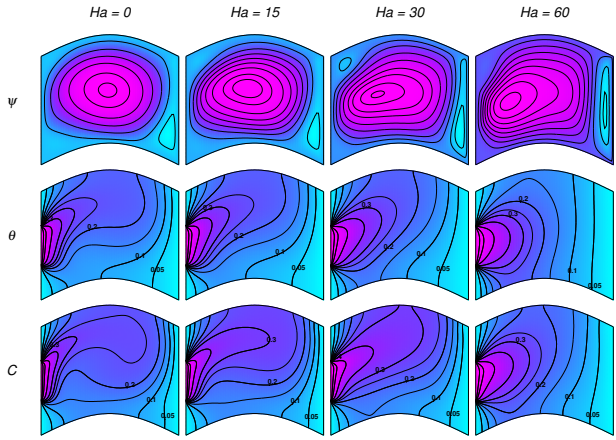

Figure 6. Streamlines, isotherms, and isoconcentrations for different Ha at $Ri = 10$, $Le = 2$, $R = 0.5$, $H = 0.4$, and $\phi = 0.01$.

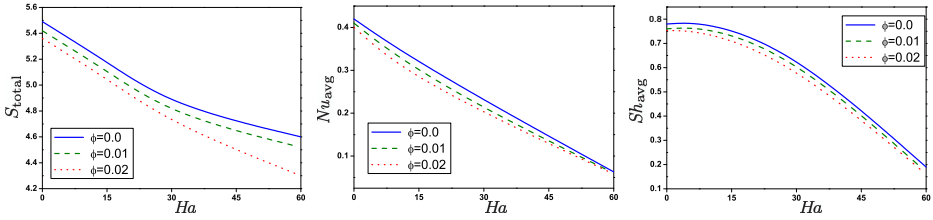

(a) (b) (c)

Figure 7. Variation of total entropy generation S_{total}, Nusselt number Nu_{avg}, and Sherwood number Sh_{avg} for different values of Ha at $Ri = 10$, $H = 0.4$, $R = 0.5$, and $Le = 2$.

field effect. In the absence of magnetic field, i.e., at $Ha = 0$, the intensity of circulation is strong and compact due to the dominant shear effect, which produces high convection mode. Further, the isotherm and isoconcentration contours are highly concentrated near heat and mass sources. But when the Hartmann number increases (i.e., $Ha = 30$ and 60), the strength of flow circulation weakens because of the presence of Lorentz force, which decelerates the flow velocity and results in an attenuation of convection mode and intensification of conduction mode. It is observed that value of $\psi_{\min} = -0.022$ for $Ha = 0$ and drops to $\psi_{\min} = -0.053$ for $Ha = 60$. The concentrated region of isotherms and isoconcentrations adjacent to the sources becomes less compressed and smooth. It is noted that the thermal boundary layer begins to fade with the ascending values of Ha. Figure 7(a) shows the variation of total entropy generated versus Ha. In our analysis, the entropy decreases when Ha increases. Therefore, we may conclude that the presence of a high value of Ha can be used to minimize entropy generation in engineering systems. Influence of Hartmann number on Nu_{avg} and Sh_{avg} is plotted in Figs. 7(b) and 7(c). Nu_{avg} and Sh_{avg} attenuate with the enhancement of Ha as the presence of a strong

magnetic field intensifies the conduction mechanism and consequently reduces the heat and mass transfer rate.

5.3 Effect of heat source location and length

The effects of heat and mass source locations R are depicted in Fig. 8 at $\phi = 0.01$, $Ha = 30$, $H = 0.4$, $Le = 2$, $Ri = 10$. The intensity of the fluid motion significantly rises when the source position moves up and also the size of the circulation cell changes. The location

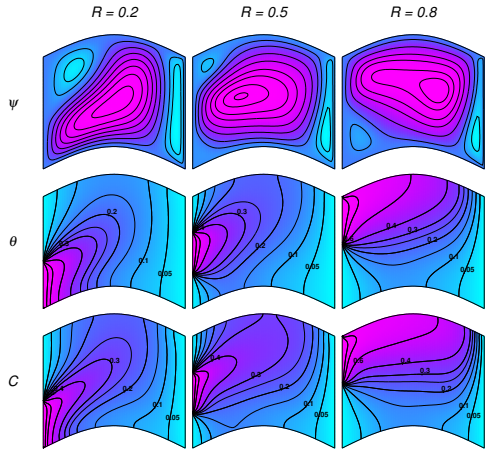

Figure 8. Streamlines, isotherms, and isoconcentrations for different heat and mass source location at $Ri = 10$, $Ha = 30$, $Le = 2$, $H = 0.4$, and $\phi = 0.01$.

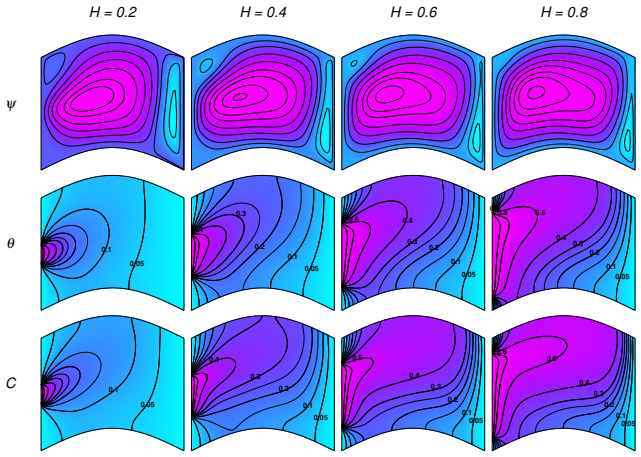

Figure 9. Streamlines, isotherms, and isoconcentrations for different heat and mass source size at $Ri = 10$, $Ha = 30$, $Le = 2$, $R = 0.5$, and $\phi = 0.01$.

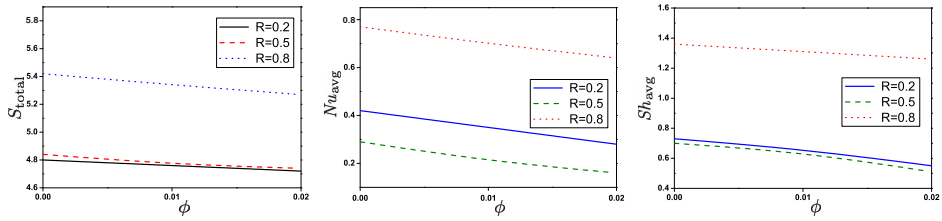

(a) (b) (c)

Figure 10. Variation of total entropy generation S_{total}, Nusselt number Nu_{avg}, and Sherwood number Sh_{avg} for different values of R at $Ri = 10$, $H = 0.4$, $Ha = 30$, and $Le = 2$.

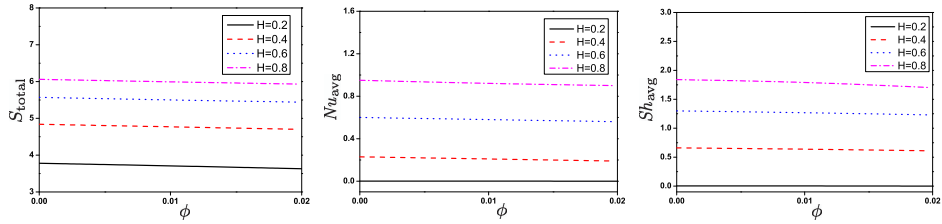

(a) (b) (c)

Figure 11. Variation of total entropy generation S_{total}, Nusselt number Nu_{avg}, and Sherwood number Sh_{avg} for different values of H at $Ri = 10$, $R = 0.5$, $Ha = 30$, and $Le = 2$.

of sources has a direct effect on the pattern of streamlines. It is found that the upper corner's circulating zones grew up and the lower corner's circulating zones dwindled by changing the source position from lower to upward. Also, the strength of isotherm and isoconcentration lines indicate that the conduction mode changes to convection mode with the increase in the source location. Numerical simulations of heat and mass source length H on the fluid flow, heat, and mass transfer are shown in Fig. 9. It is observed that when H is small, the shear-driven force is dominant as compared to the buoyancy force. The streamlines show primary clockwise circulation in the major part of the enclosure and secondary anticlockwise circulation adjacent to the cold right wall. When H increases, the buoyancy force increases considerably, which augments the circulation strength and decreases the effect of shear-driven force. The size of the primary circulation grows bigger, while the secondary circulation reduces as H increases and also the performance of the thermal process increases. The reason for all these behaviors is the total heat input that increases as the heat and mass source length increase. The temperature and concentration contours become more skewed for $H = 0.8$ due to an increase in temperature and concentration gradient with the increase in source length. Figure 10(a) presents the variation of total entropy generation with ϕ for different R. As the heat transfer rises at $R = 0.8$, the total entropy is also expected to be maximum. It is also observed that for all R, the entropy generation drops with the increase in ϕ. Figure 11(a) shows the variation of total entropy generated versus H. The total entropy generation is maximum for $H = 0.8$ due to heat transfer irreversibility, solutal concentration irreversibility, and

fluid friction irreversibility.Also, the addition of the nanoparticles to the pure fluid leads to a decrease in total entropy generation for all values of H. This happens due to an increase in viscosity that increases the fluid friction and significantly affects the entropy generation. Figures 10(b), 10(c) and 11(b), 11(c) show the variation of average Nusselt number and Sherwood number with the volume fraction of nanoparticles for different heat and mass source size and location. Both Nu_{avg} and Sh_{avg} number increase with rise in R and H. This happened because maximum temperature increases.

5.4 Effects of nanoparticle volume fraction

Figure 12 explains the effect of nanoparticles volume fraction ϕ $(0.0 \leqslant \phi \leqslant 0.02)$ on streamlines, isotherms, and isoconcentrations inside the enclosure at $Ri = 10$, $H = 0.4$, $R = 0.5$, $Ha = 30$. It is seen that the effect of the volume fraction parameter is not prominent on streamlines. The fluid motion is represented by one primary clockwise circulation and secondary counter-clockwise circulation for all cases. The increase in the nanoparticle volume fraction results in a decrease in strength of circulation. The value of $\psi_{\min} = -0.313, -0.283, -0.249$, respectively, for $\phi = 0.0, 0.01, 0.02$. This behavior is due to an increase in the fluid viscosity caused by the increase in ϕ and hence results in a decrease in flow velocity. The convection effect decreases at a high solid volume fraction of nanoparticles, and hence, the isotherms and isoconcentrations change from irregular shape for pure fluid to regular shape for nanofluid $\phi = 0.02$. A rise in ϕ enhances the thermal conductivity that consequently enhances the temperature and concentration gradient and leads to a reduction in entropy generation. Figure 13(a) shows the influence of various types of nanoparticles on total entropy generation. It is detected that the total entropy generation decreases with rising in the volume fraction of nanoparticles (Cu,

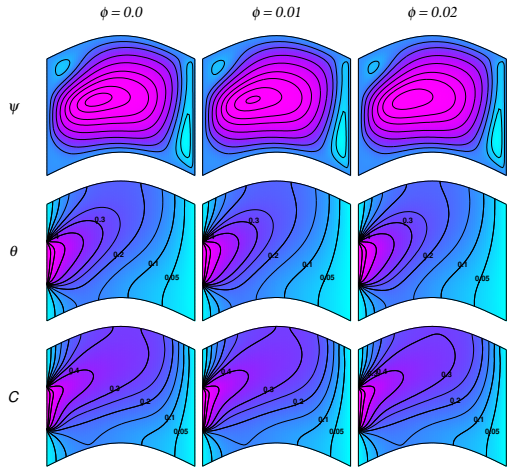

Figure 12. Streamlines, isotherms, and isoconcentrations for different volume fraction of nanoparticles at $Ri = 10$, $Ha = 30$, $Le = 2$, $R = 0.5$, and $H = 0.4$.

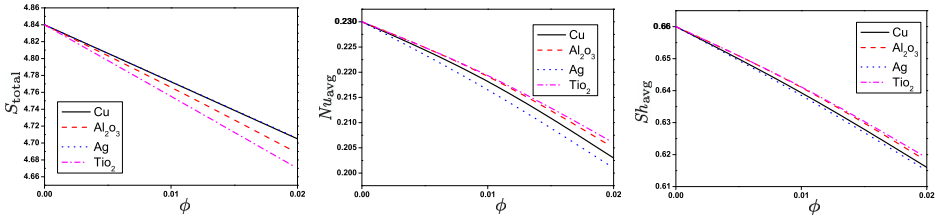

(a) (b) (c)

Figure 13. Variation of total entropy generation S_{total}, Nusselt number Nu_{avg}, and Sherwood number Sh_{avg} for different types of nanoparticles at $Ri = 10$, $R = 0.5$, $Ha = 30$, and $Le = 2$.

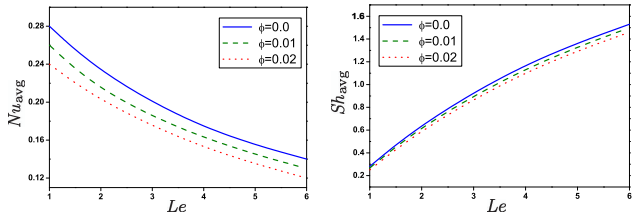

(a) (b)

Figure 14. Nusselt number Nu_{avg} and Sherwood number Sh_{avg} for different Lewis number at $Ri = 10$, $R = 0.5$, $H = 0.4$, and $Ha = 30$.

Al_2O_3, Ag, and TiO_2), and minimum entropy generation is obtained in case of TiO_2 nanoparticles. The variation of the heat and mass transfer rate is shown in Figs. 13(b) and 13(c) for various types of nanoparticles. Here we find that the highest rate of heat and mass transfer rate is obtained by adding TiO_2 compared to other nanoparticles. Due to the presence of nanoparticles, the fluid velocities decrease due to an increase in dynamic viscosity and induce resistance against the fluid motion, which in turn reduces the heat and mass transfer rate. Figures 14(a) and 14(b) show Nu_{avg} and Sh_{avg} for different Lewis number and volume fraction of nanoparticles. An increase in Le causes the solutal force to rise and tends to increase the mass transfer rate. A reverse trend is observed by the average Nusselt number, which decreases with a rise in Le.

6 Conclusion

In the present study, we have adopted a dome-shaped enclosure filled with nanofluid to study MHD double-diffusive mixed convection in the presence of discrete heating. We have considered water-based nanofluids using different types of nanoparticles. The dimensional governing equations are then converted to dimensionless forms using suitable transformations. The resulting nondimensional forms of the equations were written in stream function-velocity formulation and solved numerically using the BiCGStab method followed by the Thomas algorithm. The effect of governing parameters on the heat transfer as well as on the entropy generation is analyzed. It is found that the considered model

is convenient for entropy generation minimization. Several significant conclusions drawn from this study are listed in the following:

- An increase in Richardson number augments the strength of convection effect due to stronger buoyant force, and therefore, better enhances the heat and mass transfer rate.
- At low Richardson number, the increase in the volume fraction of nanoparticles leads to an increase in average Nusselt number, while at high Richardson number, it decreases.
- An increase in Hartmann number reduces the convection effect.
- The increase in the volume fraction of nanoparticles drops the value of stream function strongly for all values of R and H and has an adverse effect on the average Nusselt number, Sherwood number, and entropy generation.
- The heat and mass transfer rate enhances when the source length and its location increase. The increase in source length leads to an increase in the temperature inside the enclosure.
- The total entropy generation is an increasing function of Richardson number and a decreasing function of Hartmann number, volume fraction of nanoparticles, size, and location of the source.
- The highest rate of heat and mass transfer can be obtained by adding TiO_2 compared to other nanoparticles. The heat transfer rate declines with the increase of Lewis number, while the mass transfer rate increases.

The current research work can be further extended by considering the porous media and heat generation effect inside the enclosure.

Appendix

$$
\begin{aligned}
&Q_1 = \frac{\mu_{nf}}{\rho_{nf}\alpha_f}, \qquad Q_2 = \frac{(\rho\beta)_{nf}}{\rho_{nf}\beta_f}, \qquad Q_3 = \frac{\sigma_{nf}\rho_f}{\sigma_f\rho_{nf}}, \qquad Q_4 = \frac{\alpha_{nf}}{\alpha_f},\\
&a_1 = \frac{1}{J^2}\big(x_\eta^2 + y_\eta^2\big), \qquad b_1 = \frac{1}{J^2}\big(x_\xi^2 + y_\xi^2\big), \qquad e_1 = \frac{-2}{J^2}(y_\eta y_\xi + x_\eta x_\xi),\\
&c_1 = \frac{1}{J^3}\big[-y_\eta\big(\big(x_\eta^2 + y_\eta^2\big)x_{\xi\xi} - 2(y_\eta y_\xi + x_\eta x_\xi)x_{\xi\eta} + \big(x_\xi^2 + y_\xi^2\big)x_{\eta\eta}\big)\big]\\
&\qquad + \frac{1}{J^3}\big[x_\eta\big(\big(x_\eta^2 + y_\eta^2\big)y_{\xi\xi} - 2(y_\eta y_\xi + x_\eta x_\xi)y_{\xi\eta} + \big(x_\xi^2 + y_\xi^2\big)y_{\eta\eta}\big)\big],\\
&d_1 = \frac{1}{J^3}\big[-y_\xi\big(\big(x_\eta^2 + y_\eta^2\big)x_{\xi\xi} - 2(y_\eta y_\xi + x_\eta x_\xi)x_{\xi\eta} + \big(x_\xi^2 + y_\xi^2\big)x_{\eta\eta}\big)\big]\\
&\qquad + \frac{1}{J^3}\big[-x_\xi\big(\big(x_\eta^2 + y_\eta^2\big)y_{\xi\xi} - 2(y_\eta y_\xi + x_\eta x_\xi)y_{\xi\eta} + \big(x_\xi^2 + y_\xi^2\big)y_{\eta\eta}\big)\big],\\
&a_2 = a_1Q_1, \qquad b_2 = b_1Q_1, \qquad e_2 = e_1Q_1,\\
&c_2 = -\frac{1}{J}(uy_\eta - vx_\eta) + c_1Q_1, \quad d_2 = -\frac{1}{J}(-uy_\xi + vx_\xi) + d_1Q_1\\
&a_3 = a_1Q_4, \qquad b_3 = b_1Q_4, \qquad e_3 = e_1Q_4,\\
&c_3 = -\frac{1}{J}(uy_\eta - vx_\eta) + c_1Q_4, \qquad d_3 = -\frac{1}{J}(-uy_\xi + vx_\xi) + d_1Q_4
\end{aligned}
$$

$$
\begin{aligned}
a_4 &= a_1\frac{1}{Le}, \qquad b_4 = b_1\frac{1}{Le}, \quad e_4 = e_1\frac{1}{Le},\\
c_4 &= -\frac{1}{J}(uy_\eta - vx_\eta) + c_1\frac{1}{Le}, \qquad d_4 = -\frac{1}{J}(-uy_\xi + vx_\xi) + d_1\frac{1}{Le},\\
T_1 &= a_2b_1 + e_1e_2 + a_1b_2,\\
T_2 &= 2a_2e_{1\xi} + a_2d_1 + a_{1\xi}e_2 + e_{1\eta}e_2 + e_2c_1 + 2b_2a_{1\eta} + c_2e_1 + d_2a_1,\\
T_3 &= 2a_2b_{1\xi} + e_2e_{1\xi} + e_2b_{1\eta} + e_2d_1 + 2b_2e_{1\eta} + b_2c_1 + c_2b_1 + d_2e_1,\\
T_4 &= e_2b_{1\xi} + 2b_{1\eta}b_2 + b_2d_1 + d_2b_1,\\
T_5 &= e_{1\xi\xi}a_2 + 2d_{1\xi}a_2 + e_{1\xi\eta}e_2 + c_{1\xi}e_2 + d_{1\eta}e_2 + e_{1\eta\eta}b_2 + 2c_{1\eta}b_2 + e_{1\xi}c_2\\
&\quad + c_2d_1 + d_2e_{1\eta} + d_2c_1,\\
T_6 &= b_{1\xi\xi}a_2 + b_{1\xi\eta}e_2 + d_{1\xi}e_2 + b_{1\eta\eta}b_2 + 2d_{1\eta}b_2 + b_{1\xi}c_2 + b_{1\eta}d_2 + d_1d_2,\\
T_7 &= d_{1\xi\xi}a_2 + d_{1\xi\eta}e_2 + d_{1\eta\eta}b_2 + d_{1\xi}e_2 + d_{1\eta}d_2,\\
\frac{\partial\Phi}{\partial\xi} &= \frac{1}{2d}(\Phi_{i+1,j} - \Phi_{i-1,j}) + O\big(d^2\big), \qquad \frac{\partial\Phi}{\partial\eta} = \frac{1}{2d}(\Phi_{i,j+1} - \Phi_{i,j-1}) + O\big(d^2\big),\\
\frac{\partial^2\Phi}{\partial\xi^2} &= \frac{1}{d^2}(\Phi_{i+1,j} - 2\Phi_{i,j} + \Phi_{i-1,j}) + O\big(d^2\big),\\
\frac{\partial^2\Phi}{\partial\eta^2} &= \frac{1}{d^2}(\Phi_{i,j+1} - 2\Phi_{i,j} + \Phi_{i,j-1}) + O\big(d^2\big),\\
\frac{\partial^2\Phi}{\partial\xi\partial\eta} &= \frac{1}{4d^2}(\Phi_{i-1,j-1} - \Phi_{i+1,j-1} + \Phi_{i+1,j+1} - \Phi_{i-1,j+1}) + O\big(d^2\big),\\
\frac{\partial^3\Phi}{\partial\xi^3} &= \frac{1}{d^2}\big[(\Phi_\xi)_{i+1,j} - 2(\Phi_\xi)_{i,j} + (\Phi_\xi)_{i-1,j}\big] + O\big(d^2\big),\\
\frac{\partial^3\Phi}{\partial\xi^2\partial\eta} &= \frac{1}{2d^3}(2\Phi_{i,j-1} - 2\Phi_{i,j+1} - \Phi_{i-1,j-1} - \Phi_{i+1,j-1} + \Phi_{i+1,j+1} + \Phi_{i-1,j+1}) + O\big(d^2\big),\\
\frac{\partial^3\Phi}{\partial\xi\partial\eta^2} &= \frac{1}{2d^3}[2\Phi_{i-1,j} - 2\Phi_{i+1,j} - \Phi_{i-1,j-1} + \Phi_{i+1,j-1} + \Phi_{i+1,j+1} - \Phi_{i-1,j+1}] + O\big(d^2\big),\\
\frac{\partial^3\Phi}{\partial\eta^3} &= \frac{1}{d^2}\big[(\Phi_\eta)_{i,j+1} - 2(\Phi_\eta)_{i,j} + (\Phi_\eta)_{i,j-1}\big] + O\big(d^2\big),\\
\frac{\partial^4\Phi}{\partial\xi^4} &= \frac{6}{d^4}\big[d((\Phi_\xi)_{i+1,j} - (\Phi_\xi)_{i-1,j}) - 2(\Phi_{i+1,j} - 2\Phi_{i,j} + \Phi_{i-1,j})\big] + O\big(d^2\big),\\
\frac{\partial^4\Phi}{\partial\eta^4} &= \frac{6}{d^4}\big[d\big((\Phi_\eta)_{i,j+1} - (\Phi_\eta)_{i,j-1}\big) - 2(\Phi_{i,j+1} - 2\Phi_{i,j} + \Phi_{i,j-1})\big] + O\big(d^2\big),\\
\frac{\partial^4\Phi}{\partial\xi^3\partial\eta} &= \frac{1}{2d^3}\big[2(\Phi_\xi)_{i,j-1} - 2(\Phi_\xi)_{i,j+1} - (\Phi_\xi)_{i-1,j-1} - (\Phi_\xi)_{i+1,j-1}\\
&\quad + (\Phi_\xi)_{i+1,j+1} + (\Phi_\xi)_{i-1,j+1}\big] + O\big(d^2\big),\\
\frac{\partial^4\Phi}{\partial\xi\partial\eta^3} &= \frac{1}{2d^3}\big[2(\Phi_\eta)_{i-1,j} - 2(\Phi_\eta)_{i+1,j} - (\Phi_\eta)_{i-1,j-1} + (\Phi_\eta)_{i+1,j-1}\\
&\quad + (\Phi_\eta)_{i+1,j+1} - (\Phi_\eta)_{i-1,j+1}\big] + O\big(d^2\big),\\
\frac{\partial^4\Phi}{\partial\xi^2\partial\eta^2} &= \frac{1}{d^4}\big[4\Phi_{i,j} - 2(\Phi_{i-1,j} + \Phi_{i+1,j} + \Phi_{i,j-1} + \Phi_{i,j+1}) + \Phi_{i-1,j-1}\\
&\quad + \Phi_{i+1,j-1} + \Phi_{i+1,j+1} + \Phi_{i-1,j+1}\big] + O\big(d^2\big),
\end{aligned}
$$

where the discretization of any function Φ (such as ψ, θ, C, etc.) is shown, and d is the step length on a uniform rectangular mesh in the transformed domain.

References

1. S.E. Ahmed, Natural convection of dusty hybrid nanofluids in diverging-converging cavities including volumetric heat sources, *J. Therm. Sci. Eng. Appl.*, **13**(1):011018, 2021, https://doi.org/10.1115/1.4047275.
2. L.M. Al-Balushi, M.J. Uddin, M.M. Rahman, Natural convective heat transfer in a square enclosure utilizing magnetic nanoparticles, *Propul. Power Res.*, **8**(3):194–209, 2019, https://doi.org/10.1016/j.jppr.2018.07.009.
3. S.M. Aminossadati, B. Ghasemi, Natural convection cooling of a localised heat source at the bottom of a nanofluid-filled enclosure, *Eur. J. Mech., B, Fluids*, **28**(5):630–640, 2009, https://doi.org/10.1016/j.euromechflu.2009.05.006.
4. A.A.A. Arani, A. Ababaei, G.A. Sheikhzadeh, A. Aghaei, Numerical simulation of double-diffusive mixed convection in an enclosure filled with nanofluid using Bejan's heatlines and masslines, *Alexandria Eng. J.*, **57**(3):1287–1300, 2018, https://doi.org/10.1016/j.aej.2017.03.034.
5. S. Bezi, B. Souayeh, N. Ben-Cheikh, B. Ben-Beya, Numerical simulation of entropy generation due to unsteady natural convection in a semi-annular enclosure filled with nanofluid, *Int. J. Heat Mass Transfer*, **124**:841–859, 2018, https://doi.org/10.1016/j.ijheatmasstransfer.2018.03.109.
6. H.C. Brinkman, The viscosity of concentrated suspensions and solutions, *J. Chem. Phys.*, **20**(4):571–581, 1952, https://doi.org/10.1063/1.1700493.
7. A.J. Chamkha, M.A. Mansour, A.M. Rashad, H. Kargarsharifabad, T. Armaghani, Magnetohydrodynamic mixed convection and entropy analysis of nanofluid in Gamma-Shaped porous cavity, *J. Thermophys. Heat Transf.*, **34**(10):1–12, 2020, https://doi.org/10.2514/1.T5983.
8. P.K. Das, S. Mahmud, Numerical investigation of natural convection inside a wavy enclosure, *Int. J. Therm. Sci.*, **42**(4):397–406, 2003, https://doi.org/10.1016/S1290-0729(02)00040-6.
9. M. Ghalambaz, A. Doostani, E. Izadpanahi, A.J. Chamkha, Conjugate natural convection flow of Ag-MgO/water hybrid nanofluid in a square cavity, *J. Therm. Anal. Calorm.*, **139**:2321–2336, 2020, https://doi.org/10.1007/s10973-019-08617-7.
10. B. Ghasemi, S.M. Aminossadati, A. Raisi, Magnetic field effect on natural convection in a nanofluid-filled square enclosure, *Int. J. Therm. Sci.*, **50**(9):1748–1756, 2011, https://doi.org/10.1016/j.ijthermalsci.2011.04.010.
11. M.M. Gupta, J.C. Kalita, A new paradigm for solving Navier-Stokes equation: Streamfunction-vorticity formulation, *J. Comput. Phys.*, **207**:52–68, 205, https://doi.org/10.1016/j.jcp.2005.01.002.
12. S. Izadi, T. Armaghani, R. Ghasemiasl, A.J. Chamkha, M. Molana, A comprehensive review on mixed convection of nanofluids in various shapes of enclosures, *Powder Technol.*, **343**:880–907, 2019, https://doi.org/10.1016/j.powtec.2018.11.006.

13. S. Kashani, A.A. Ranjbar, M. Mastiani, H. Mirzaei, Entropy generation and natural convection of nanoparticle-water mixture (nanofluid) near water density inversion in an enclosure with various patterns of vertical wavy walls, *Appl. Math. Comput.*, **226**:180–193, 2014, https://doi.org/10.1016/j.amc.2013.10.054.

14. C.T. Kelley, *Iterative Methods for Linear and Nonlinear Equations*, SIAM, Philadelphia, 1995.

15. M.K. Koopaee, A. Omidvar, I. Jelodari, Numerical study on the steady-state heat transfer rate of nanofluid filled within square cavity in the presence of oriented magnetic field, *Proc. Inst. Mech. Eng., Part C, J. Mech. Eng. Sci.*, **228**(8):1348–1362, 2012, https://doi.org/10.1177/0954406213507860.

16. T. Mahalakshmi, N. Nithyadevi, H.F. Öztop, N. Abu-Hamdeh, Natural convective heat transfer of Ag-water nanofluid flow inside enclosure with center heater and bottom heat source, *Chin. J. Phys.*, **56**(4):1497–1507, 2018, https://doi.org/10.1016/j.cjph.2018.06.006.

17. T.R. Mahapatra, D. Pal, S. Mondal, Natural convection in a lid-driven square cavity filled with Darcy-Forchheimer porous medium in the presence of thermal radiation, *Int. J. Nonlinear Sci.*, **11**(3):366–379, 2011.

18. T.R. Mahapatra, D. Pal, S. Mondal, Effects of buoyancy ratio on double-diffusive natural convection in a lid-driven cavity, *Int. J. Heat Mass Transfer*, **57**(2):771–785, 2013, https://doi.org/10.1016/j.ijheatmasstransfer.2012.10.028.

19. T.R. Mahapatra, D. Pal, S. Mondal, Mixed convection flow in an inclined enclosure under magnetic field with thermal radiation and heat generation, *Int. Commun. Heat Mass Transfer*, **41**:47–56, 2013, https://doi.org/10.1016/j.icheatmasstransfer.2012.10.028.

20. T.R. Mahapatra, R. Parveen, Entropy generation in MHD natural convection within curved enclosure filled with Cu-water nanofluid, *J. Nanofluids*, **8**(5):37–47, 2019, https://doi.org/10.1166/jon.2019.1646.

21. S. Mahmud, A.K.M. Sadrul Islam, Laminar free convection and entropy generation inside an inclined wavy enclosure, *Int. J. Therm. Sci.*, **42**(11):1003–1012, 2003, https://doi.org/10.1016/S1290-0729(03)00076-0.

22. J.C. Maxwell, *A Treatise on Electricity and Magnetism, Vol. II*, Clarendon Press, Oxford, 1873.

23. S.A.M. Mehryan, M. Ghalambaz, A.J. Chamkha, M. Izadi, Numerical study on natural convection of Ag-MgO hybrid/water nanofluid inside a porous enclosure: A local thermal non-equilibrium model, *Powder Technol.*, **367**:443–455, 2020, https://doi.org/10.1016/j.powtec.2020.04.005.

24. M. Molana, A.S. Dogonchi, T. Armaghani, A.J. Chamkha, D.D. Ganji, I. Tlili, Investigation of hydrothermal behavior of Fe_3O_4-H_2O nanofluid natural convection in a novel shape of porous cavity subjected to magnetic field dependent (MFD) viscosity, *J. Energy Storage*, **30**:101395, 2020, https://doi.org/10.1016/j.est.2020.101395.

25. P. Mondal, T.R. Mahapatra, Minimization of entropy generation due to MHD double diffusive mixed convection in a lid driven trapezoidal cavity with various aspect ratios, *Nonlinear Anal. Model. Control*, **25**(4):545–563, 2020, https://doi.org/10.15388/namc.2020.25.16774.

26. H.F. Öztop, K. Al-Salem, A review on entropy generation in natural and mixed convection heat transfer for energy systems, *Renewable and Sustainable Energy Rev.*, **16**(1):911–920, 2012, https://doi.org/10.1016/j.rser.2011.09.012.

27. R. Parveen, T.R. Mahapatra, Numerical simulation of MHD double diffusive natural convection and entropy generation in a wavy enclosure filled with nanofluid with discrete heating, *Heliyon*, **5**(9):e02496, 2019, https://doi.org/10.1016/j.heliyon.2019.e02496.

28. N. Rahimpour, M.K. Moraveji, Free convection of water-Fe_3O_4 nanofluid in an inclined cavity subjected to a magnetic field: CFD modeling, sensitivity analysis, *Adv. Powder Technol.*, **28**(6):1573–1584, 2017, https://doi.org/10.1016/j.apt.2017.03.029.

29. Z.Z. Rashed, M.A. Mansour, M.A. Attia, S.E. Ahmed, Numerical study of radiative impacts on a magneto-convective flow confined an inclined two-sided wavy enclosure using hybrid nanofluid, *Phys. Scr.*, **96**(2):025216, 2021, https://doi.org/10.1088/1402-4896/abd1b1.

30. M. Sheikholeslami, M.G. Bandpy, R. Ellahi, A. Zeeshan, Simulation of MHD CuO-water nanofluid flow and convective heat transfer considering lorentz forces, *J. Magn. Magn. Mater.*, **369**:69–80, 2014, https://doi.org/10.1016/j.jmmm.2014.06.017.

31. M. Sheikholeslami, M. Gorji-Bandpy, D.D. Ganji, S. Soleimani, Natural convection heat transfer in a cavity with sinusoidal wall filled with CuO-water nanofluid in presence of magnetic field, *J. Taiwan Inst. Chem. Eng.*, **45**(1):40–49, 2014, https://doi.org/10.1016/j.jtice.2013.04.019.

32. M.A. Teamah, M.M. Sorour, W.M. El-Maghlany, A. Afifi, Numerical simulation of double diffusive laminar mixed convection in shallow inclined cavities with moving lid, *Alexandria Eng. J.*, **52**(3):227–239, 2013, https://doi.org/10.1016/j.aej.2013.02.001.

33. M.B. Uddin, M. Rahman, M. Khan, R. Saidur, T.A. Ibrahim, Hydromagnetic double-diffusive mixed convection in trapezoidal enclosure due to uniform and nonuniform heating at the bottom side: Effect of Lewis number, *Alexandria Eng. J.*, **55**(2):1165–1176, 2016, https://doi.org/10.1016/j.aej.2016.03.035.

34. Y. Xuan, Q. Li, Heat transfer enhancement of nanofluids, *Int. J. Heat Fluid Flow*, **21**(1):58–64, 2000, https://doi.org/10.1016/S0142-727X(99)00067-3.

35. A. Zaim, A. Aissa, F. Mebarek-Oudinac, B. Mahanthesh, G. Lorenzini, M. Sahnoun, M. El Ganaoui, Galerkin finite element analysis of magneto-hydrodynamic natural convection of Cu-water nanoliquid in a baffled U-shaped enclosure, *Propul. Power Res.*, **9**(4):383–393, 2020, https://doi.org/10.1016/j.jppr.2020.10.002.